GENERATION OF AVAILABLE POTENTIAL ENERGY AND THE ENERGY CYCLE DURING THE GLOBAL WEATHER EXPERIMENT

First year final report on contract number NAS5-27745

David A. Salstein
Richard D. Rosen

Atmospheric and Environmental Research, Inc.
840 Memorial Drive
Cambridge, Massachusetts 02139

February 1985

1. Introduction

Gridded analyses of the state of the atmosphere during part of the Global Weather Experiment (FGGE) have been produced by a special objective analysis system (Baker, 1983) incorporated within the Goddard Laboratory for Atmospheres (GLA) Fourth Order General Circulation Model (Kalnay et al., 1983). In our previous contract (NAS5-26515) we utilized one month of these analyses during the First Special Observing Period to determine large-scale circulation statistics, including estimates of certain components of the energy cycle. In that study, in fact, we examined two parallel sets of analyses, which in one case included and in the other omitted data observed by satellite-based and other FGGE special observing systems. This contract year, we have extended the results of our previous work in two separate, but not unrelated, ways.

(a) First, from these two parallel analyses, which we labeled FGGE (full FGGE system) and NOSAT (satellite omitted), we discovered that, by and large, the two sets of fields were quite close over much of the globe. Nevertheless, locally the influence of satellite-based systems led to some differences, particularly over the Southern Hemisphere oceans.

Upon examining the differences between the FGGE and NOSAT cases, the question arose concerning whether the GLA model itself was playing a large role in producing features in the analysis fields, independent of the assimilated input data. To answer that question, the GLA model was run again for the same time period in a special way: after being started with an initial state, no observations were assimilated for the duration of the run. This method produces fields which define the "climate" of the model, with which the data assimilation runs can be compared.

(b) As the second thrust of the work this year, we have been examining the diabatic heating fields generated by the GLA FGGE analysis. From these fields, one can ascertain the role of total diabatic heating and of the various diabatic heating components in the atmospheric energy cycle, in particular in the generation of available potential energy. To date, we have accumulated fields of four components of diabatic heating for the month study period and are preparing to use them further for the energetics study.

2. The CLIMATE run

The GLA model was initialized from the European Centre for Medium Range Weather Forecasts (ECMWF) analysis of December 15, 1978 at 00 GMT and was

permitted to run for a period of 50 days without incorporating any input data. For the last 30 days of this run time, equivalent to the monthly period of January 6 - February 4, we were supplied with analysis fields of raw meteorological parameters at 00 GMT. Each parameter was averaged separately for the entire month at each point of the 4° x 5° latitude-longitude global grid at the 12 pressure levels 1000, 850, 700, 500, 400, 300, 250, 200, 150, 100, 70 and 50 mb. After the 20-day "start-up" period, the model fields are thought to have very little influence of the original state, but instead reflect the characteristics of the model itself. We label the average of such analysis the "climate" of the model.

We have chosen to look at mean fields of zonal wind, $\bar{u}$, meridional wind, $\bar{v}$, and temperature, $\bar{T}$, and the quantities related to transient eddy components of meridional transports of momentum and heat, $\overline{u'v'}$ and $\overline{v'T'}$ respectively. Here the overbar indicates the monthly mean, while the prime denotes departure from that mean. All fields were restricted to the portion of the globe north of 68°S. To the south of that latitude, the high topography of Antarctica affects the low-level fields.

In Figure 1 are plotted the monthly averages of u at 200 mb for the (a) FGGE, (b) NOSAT and (c) CLIMATE analyses. Areas not shaded are westerlies; shaded areas are easterlies. In general, the features are similar in the three analyses. However, maxima in the winds seem to be somewhat stronger in the NOSAT analysis than in the FGGE analysis; examples of this are found in the jet maxima off the coasts of Japan and North America and also over the Southern Hemisphere oceans. The CLIMATE case yields even stronger features. In fact, the strong feature south of Australia in the CLIMATE run is considerably stronger than winds in that region as diagnosed by the two data-assimilation runs. It can be seen by comparing the NOSAT field to the CLIMATE field that the effect of adding conventional data to analyses produced by the model climate is to dampen the zonal winds considerably. The further impact of adding the satellite-based data (forming the FGGE field) is to dampen these winds a bit further. This general impact on the zonal winds can be seen as well in Figure 2 where the cross-section of zonally averaged zonal winds, $[\bar{u}]$, is displayed. (Brackets denote the zonal average of a quantity.) Thus, the maxima in the jet regions in the CLIMATE run are stronger than in either of the data assimilation runs, and, in the Northern Hemisphere in particular, the strong CLIMATE winds extend to lower levels in the atmosphere.

As for the meridional circulation, Figure 3 shows the distributions of $\bar{v}$ at 200 mb for the three cases. Unlike the situation for $\bar{u}$, there appears to be no consistent picture of the relative strengths among the three cases of the $\bar{v}$ analyses. One area where upper atmosphere meridional winds are stronger in the CLIMATE case than in the others exists, for example, in eastern Asia. The reverse situation, however, seems to occur over much of South America. In the latitude-pressure cross section of Figure 4, the zonally averaged mass streamfunction associated with the meridional winds is shown. Here we see a weaker Northern Hemisphere (winter) Hadley cell in the CLIMATE case, but a somewhat stronger midlatitude indirect cell. Thus, there is no single effect of data assimilation even on the zonally averaged meridional circulation.

In the case of the temperature field, the maxima and minima tend in general not to be as extreme in the CLIMATE run as in the others. Figure 5 illustrates this observation at the 850 mb level, in particular over central Siberia and Canada for minima, and western Australia, south and east Africa for maxima. This is not the case, however, for west Africa, in the vicinity of the Sahara, where very high values exist in the CLIMATE run. The atmosphere above the Southern Hemisphere mid-latitude oceans appears to be somewhat colder in the CLIMATE run. A zonal cross section of the temperature field (Figure 6) shows that the CLIMATE analyses are somewhat different from the others, especially in the high latitudes of both hemispheres. There, in the CLIMATE run, the highest levels are colder, while the lowest levels are warmer.

Figures 7 and 8 contain quantities related to the transient eddy transport of momentum at 200 mb and that of heat at 850 mb, respectively, for the three analyses. One interesting feature in $\overline{u'v'}$ is the strong center in the Pacific off the coast of North America, apparent in the FGGE, NOSAT, and CLIMATE cases, but absent in a separate analysis not involving the GLA model but based on rawinsonde and pilot balloon station data (see Figure 17 of Salstein and Rosen, 1982). This feature, generated by the GLA model climate, may also be captured in the NOSAT and FGGE analyses by aircraft observations, but further investigation would be necessary to examine these observations for confirmation of the feature.

Thus, the results of comparing the data assimilation runs to the CLIMATE run are mixed. In many cases, the CLIMATE values are rather different from the FGGE and NOSAT values, which are themselves quite close; this indicates

that the model climate does not dominate in forcing features of the analyses. Such a case can be observed, for example, in the $\bar{u}$ field at 200 mb to the south of Australia. However, some influences of the climatology of the model are seen in the data assimilation runs, such as the feature noted above in the $\overline{u'v'}$ field off the coast of North America.

3. Diabatic heating fields

The GLA 4-dimensional model and data assimilation system were rerun for our study period for the purpose of archiving a number of parameters related to the model physics. Of these, we were interested in those important with regard to the diabatic heating occurring within the model. Components of diabatic heating are computed diagnostically every 30 minutes of model time, and these were accumulated so that heating by the various components within every six hour period is archived in units of $^{\circ}K\ day^{-1}$. The particular quantities archived for the quarter-days ending 0, 6, 12 and 18 GMT were fields of heating due to shortwave radiation, Q_{SW}, sensible heating, Q_S, and latent heating, Q_L, as well as the total diabatic heating, Q_T. The fourth component of diabatic heating, that due to longwave radiation, Q_{LW}, was not archived in the same manner, and so was recovered by means of taking the difference between the total diabatic heating and the other three components:

$$Q_{LW} = Q_T - (Q_{SW} + Q_S + Q_L)$$

The diabatic heating fields are produced and archived on the non-dimensional "σ" vertical coordinate system (Kalnay et al., 1983). As such, they are representative of 9 equal-pressure layers from 10 mb to the surface and are given at the midpoints of these layers. In the σ system, pressure is variable for each day as well as for each gridpoint, and so it is not a good system in which to form monthly sums. We have therefore chosen to transform the data onto the same number of pressure (p) surfaces and have picked for that purpose the 9 convenient levels: 1000, 925, 850, 700, 500, 400, 300, 200 and 100 mb. In making the transformation from σ to p coordinates, the data at each gridpoint for each day were interpolated or extrapolated linearly in the logarithm of pressure onto the chosen pressure levels. If a gridpoint was below the surface topography at some level, no data value was given there for the day. Finally, for each of the four synoptic hours separately, for the

temperature field, each of the heating fields and their cross products (and some other related quantities -- see Table 1), we formed sums of the values at all locations of the three dimensional grid, when available. In addition, the number of data values forming these sums was stored so that mean values could be computed.

In the next set of figures are presented monthly mean fields of the diabatic heating components as well as the total diabatic heating for the four synoptic hours, as derived by the method described above. The heating fields are presented at both a lower and middle level of the atmosphere (850 mb and 500 mb, respectively).

Figures 9 and 10 show the heating due to shortwave radiation at the two pressure levels; units are °K day^{-1}, with values of 0 (no heating) shaded and isolines at 1 °K day^{-1}. Figures 11 and 12 show longwave radiative heating sensible heating fields appear in Figures 13 and 14, and latent heating in Figures 15 and 16. In Figures 17 and 18 are fields of the total diabatic heating for the four synoptic hours, equal to the sum of the four components. The heating components have been averaged for the four synoptic hours in Figures 19 and 20 (labeled "24 hours"), and the 24-hour total diabatic heating appears in Figures 21 and 22. In all fields other than shortwave heating, negative values, or areas of cooling, are shaded, and isolines are 2 °K day^{-1}.

The shortwave heating fields show the daily progression of the sun about the earth's longitudes during this time period. At grid locations below the topography, such as occurs at 850 mb in high areas of the Himalayas, Rockies, Andes, and Antarctica, heating values are simply considered to be zero. These areas are shaded in the maps of the shortwave heating field.

The longwave heating fields are negative everywhere above the topography, with maximum cooling occurring in the tropics. There appears to be less of a diurnal cycle noticeable in these fields, in comparison with shortwave heating.

Sensible heating is strongly dependent at the lower level on the land/ocean distribution and time of day, largely cooling over the continents during the night and heating during the day. There are some very strong values at 850 mb over east Africa, Australia, and South America during local afternoon. At 500 mb, sensible heating is mostly negative, with some small positive regions observed.

Lastly, latent heating is weaker at 850 mb than 500 mb. At both levels, the region of cooling due to evaporation is smaller than the region of heating due to condensation. At the 500 mb level there are maxima in the equatorial region and some very intense heating areas, particularly over the Indonesian region and South America.

We see a clear distinction between the four synoptic hours in the total diabatic heating fields (Figures 17 and 18). This diurnal signal in total heating appears to be dominated by the sensible heating and shortwave radiative heating processes, in that they produce their heating locally at particular times of the day.

In comparing the four 24-hour component heating fields (Figures 19 and 20), we see in particular the importance of strong latent heating at the 500 mb level, and both latent and sensible heating lower down at 850 mb. These, however, are more than balanced in most areas by the strong cooling due to longwave radiation. Shortwave radiative heating is relatively weak everywhere.

The 24-hour total diabatic heating fields (Figures 21 and 22) show heating across much of the tropics at 850 mb, which is especially strong over the land areas of South America, Africa, and Indonesia-Australia. Residuals of these heating areas still appear at the 500 mb level. However, most of the globe is covered at both levels by areas of less intense cooling.

4. Concluding remarks.

In our continuing efforts, we will use the diabatic heating fields shown in the previous section to estimate their role in the generation of available potential energy. These components of the energy cycle will be calculated in both zonal mean form, $G(P_M)$, and eddy form, $G(P_E)$. These are terms within the atmospheric energy cycle which were not possible to calculate from the NASA GLA data prior to the archival of the heating components from the FGGE run.

An approximate formulation of the two G terms was originally given by Lorenz and is shown below in the framework of Peixoto and Oort (1974). This traditional approach involves the calculation of the G terms from the horizontally averaged static stability factor γ and the various heating fields:

$$G(P_M) = \iint \gamma(p)\ [\overline{T}]''\ [\overline{Q}]''\ dm$$

$$G(P_E) = G(P_{TE}) + G(P_{SE}) = \iint \gamma(p)\ ([\overline{T'Q'}] + [\overline{T}^*\overline{Q}^*])\ dm$$

where $[\overline{T}]'' = [\overline{T}] - \int [\overline{T}] \cos\phi\ d\phi$,

is a departure from a hemispheric or global mean. The asterisk denotes a departure from zonal mean and dm is an element of mass. As indicated above, we will consider the generation of potential eddy by both transient eddies (TE) and standing eddies (SE).

A more exact form of the generation terms based on Boer (1975) will also be calculated as follows:

$$G(P_M) = \iint [\overline{N}][\overline{Q}]\ dm$$

$$G(P_E) = \iint \gamma(\phi,p) \cdot ([\overline{T'Q'}] + [\overline{T}^*\overline{Q}^*])\ dm$$

Here $[\overline{N}]$ is an "efficiency factor" (see Lorenz, 1963) and the stability factor γ is based upon latitude as well as pressure. The results obtained from this more exact approach will be compared with those from the Lorenz approximation. In this way, a number of estimates of the previously unavailable generation terms will be obtained.

5. References

Baker, W.E., 1983: Objective analysis and assimilation of observational data from FGGE. Mon. Wea. Rev., 111, 328-342.

Boer, G.J., 1975: Zonal and eddy forms of the available potential energy equations in pressure coordinates. Tellus, 27, 433-442.

Kalnay, E., R. Balgovind, W. Chao, D. Edelmann, J. Pfaendtner, L. Takacs, and K. Takano, 1983: Documentation of the GLAS fourth-order general circulation model. NASA Technical Memorandum 86064.

Lorenz, E.N., 1963: The Nature and Theory of the General Circulation of the Atmosphere. World Meteorological Organization, 161 pp.

Peixoto, J.P. and A.H. Oort, 1974: The annual distribution of atmospheric energy on a planetary scale. J. Geophys. Res., 79, 2149-2159.

Salstein, D.A. and R.D. Rosen, 1982: Impact of satellite data on large-scale circulation statistics as determined from GLAS analyses during FGGE SOP-I. Final report, NASA contract NAS5-26515.

Table 1

Quantities relating to diabatic heating fields.
Averages formed for January 6 - February 4, 1979.

Quantity		
1	T	(temperature, °K)
2	Q_{SW}	(heating due to shortwave radiation, °K day^{-1})
3	Q_{LW}	(heating due to longwave radiation, °K day^{-1})
4	Q_S	(sensible heating, °K day^{-1})
5	Q_L	(latent heating, °K day^{-1})
6	$T \cdot Q_{SW}$	
7	$T \cdot Q_{LW}$	
8	$T \cdot Q_S$	
9	$T \cdot Q_L$	
10	T^2	
11	Q_{SW}^2	
12	Q_{LW}^2	
13	Q_S^2	
14	Q_L^2	
15	Q_T^2	(total heating^2)
16	Number of time periods grid point is above topography	
17	ω	(vertical velocity, 10^{-6} mb s^{-1})
18	p_s	(surface pressure = reference pressure + 10 mb)

Total heating: $Q_T = Q_{SW} + Q_{LW} + Q_S + Q_L$

$TQ_T = TQ_{SW} + TQ_{LW} + TQ_S + TQ_L$

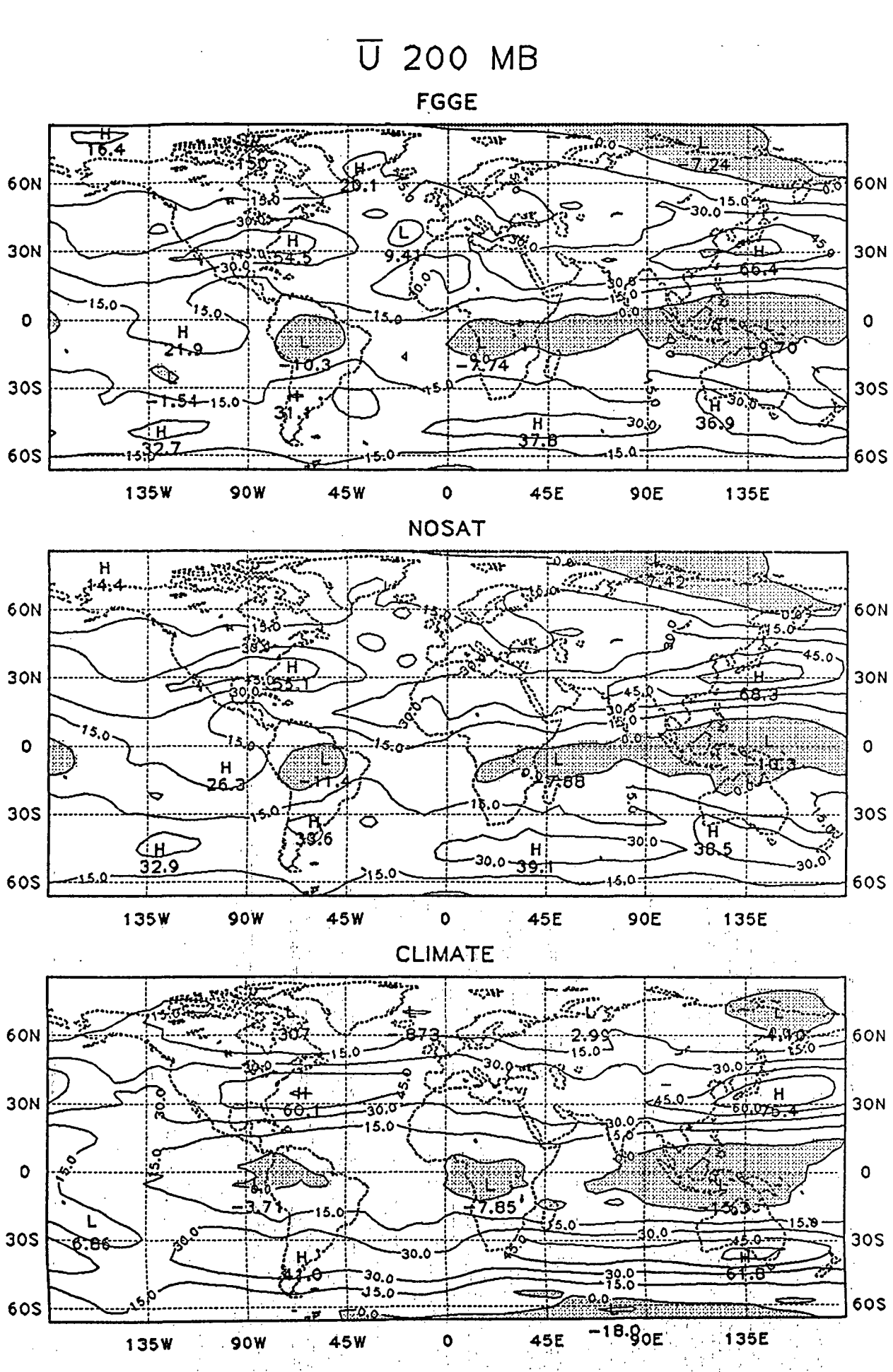

Figure 1. Zonal wind ($\bar{u}$) in m s^{-1} at 200 mb for the FGGE, NOSAT and CLIMATE analyses. Westerlies are positive; easterlies (shaded) are negative.

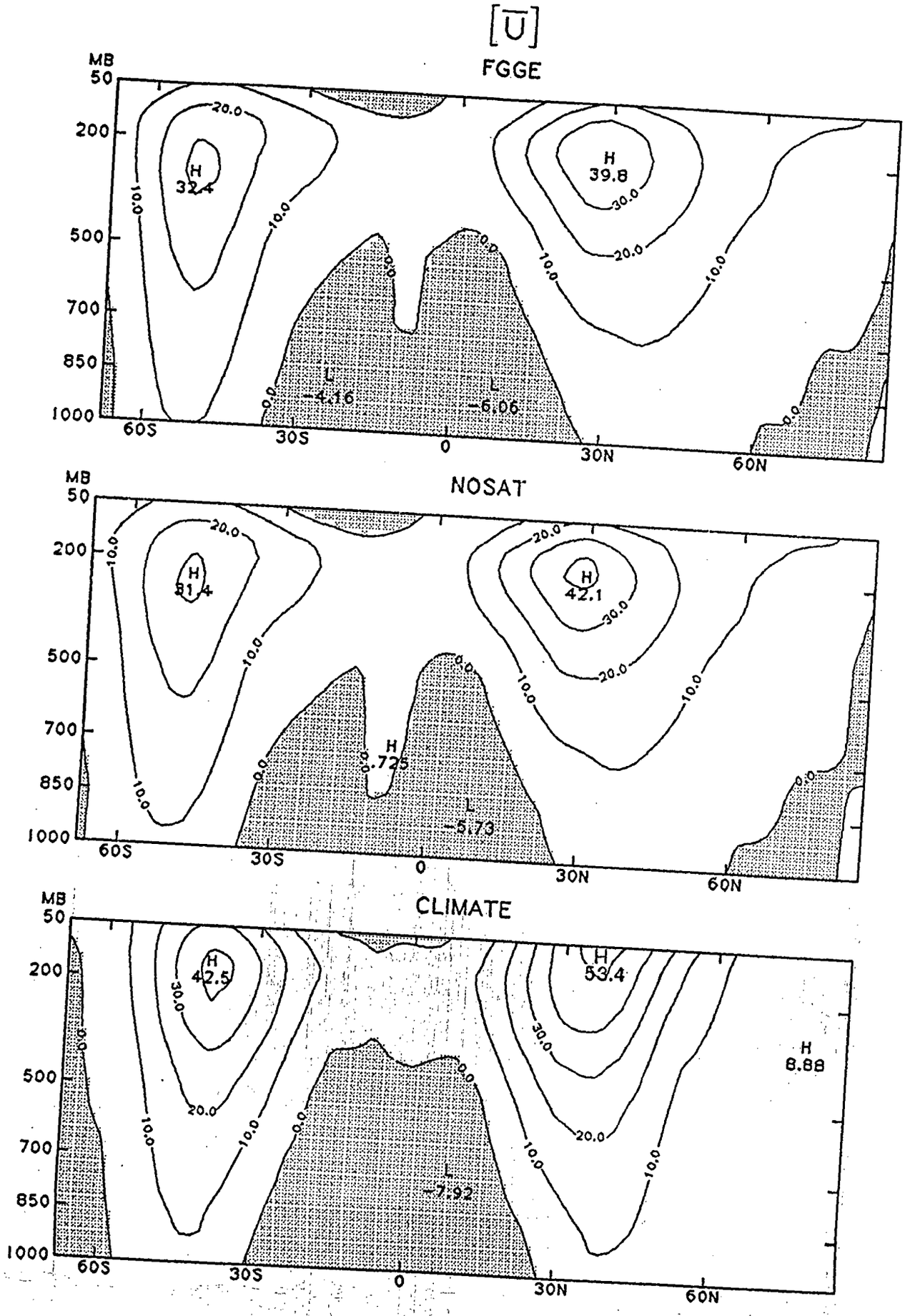

Figure 2. Zonally averaged zonal wind ($[\bar{u}]$) for the FGGE, NOSAT and CLIMATE analyses. Westerlies are positive, easterlies (shaded) are negative.

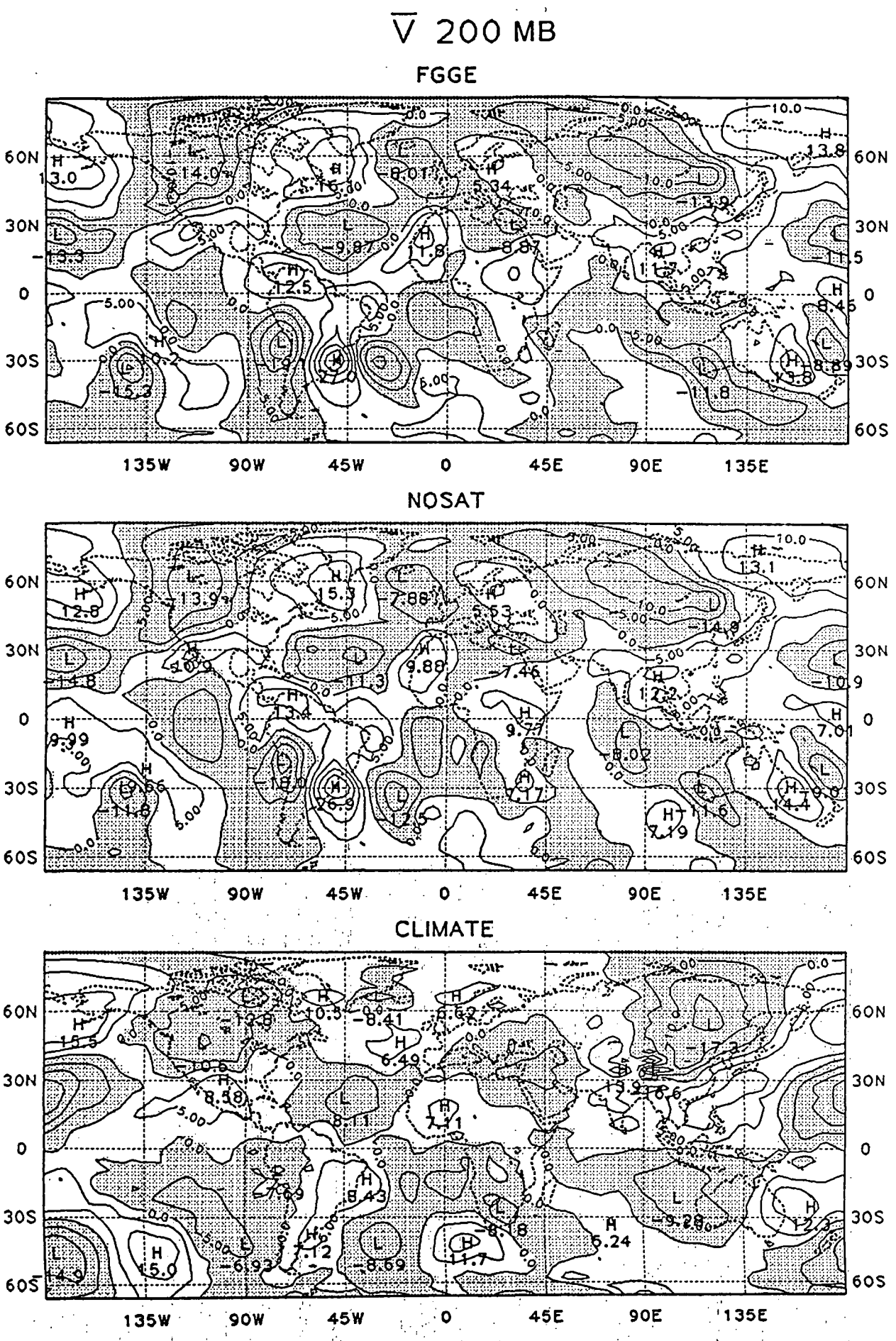

Figure 3. Meridional wind ($\bar{v}$) in m s^{-1} at 200 mb for the FGGE, NOSAT and CLIMATE analyses. Southerlies are positive; northerlies (shaded) are negative.

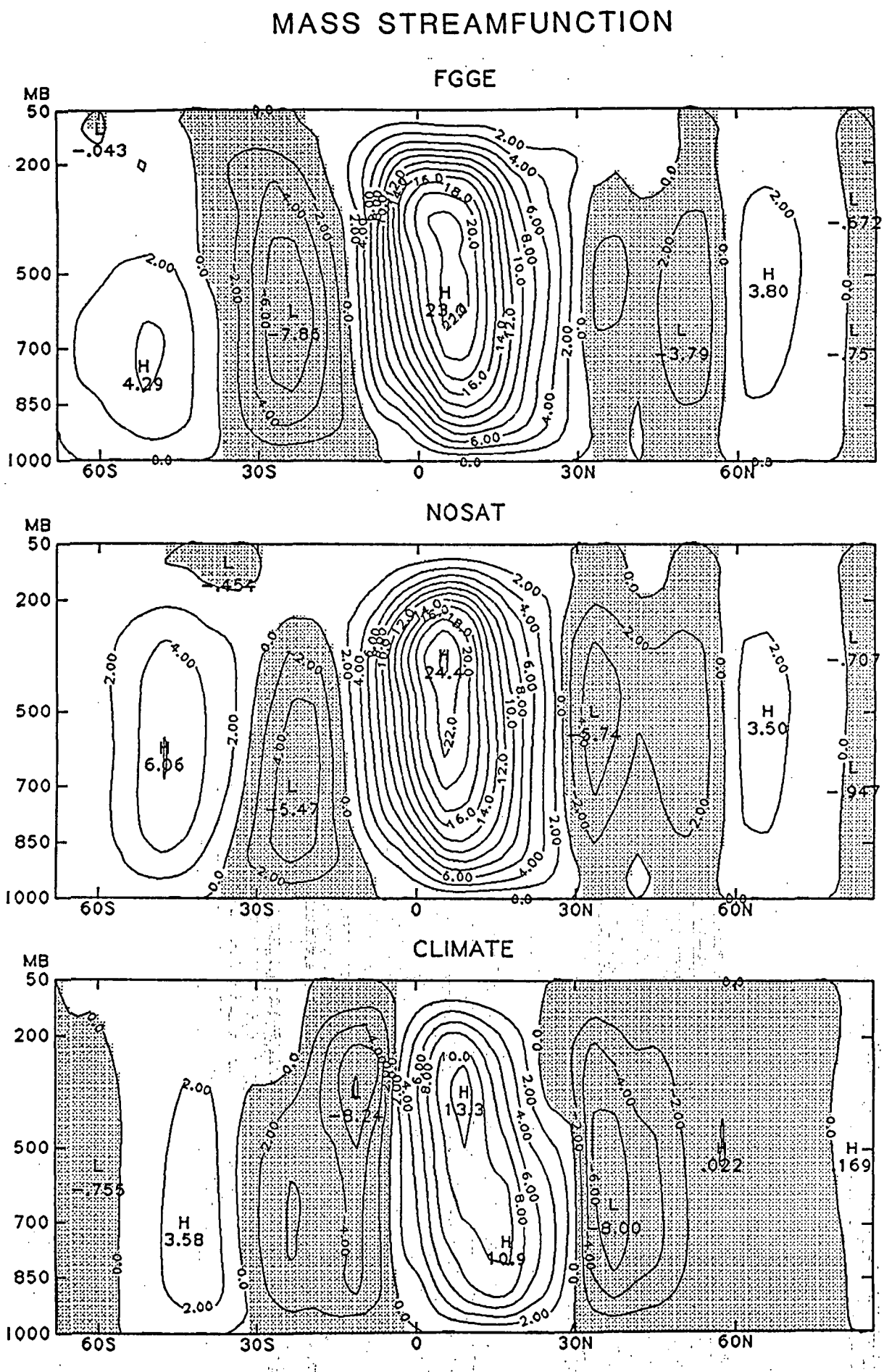

Figure 4. Mass streamfunction ($\bar{\psi}$) of the meridional-vertical zonally averaged flow in 10^{10} kg s^{-1} for the FGGE, NOSAT, and CLIMATE analyses.

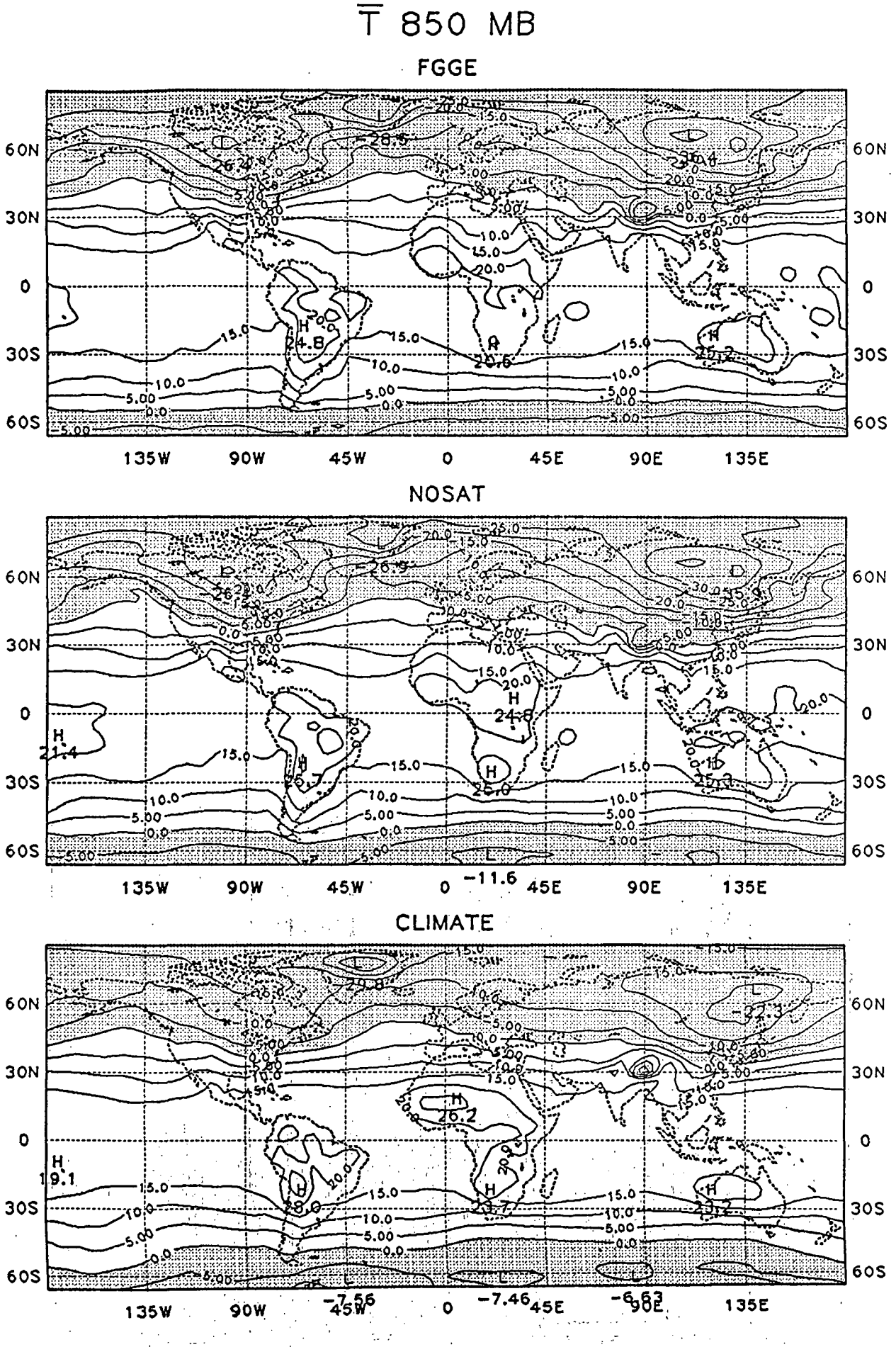

Figure 5. Temperature ($\overline{T}$) in °C at 850 mb for the FGGE, NOSAT, and CLIMATE analyses.

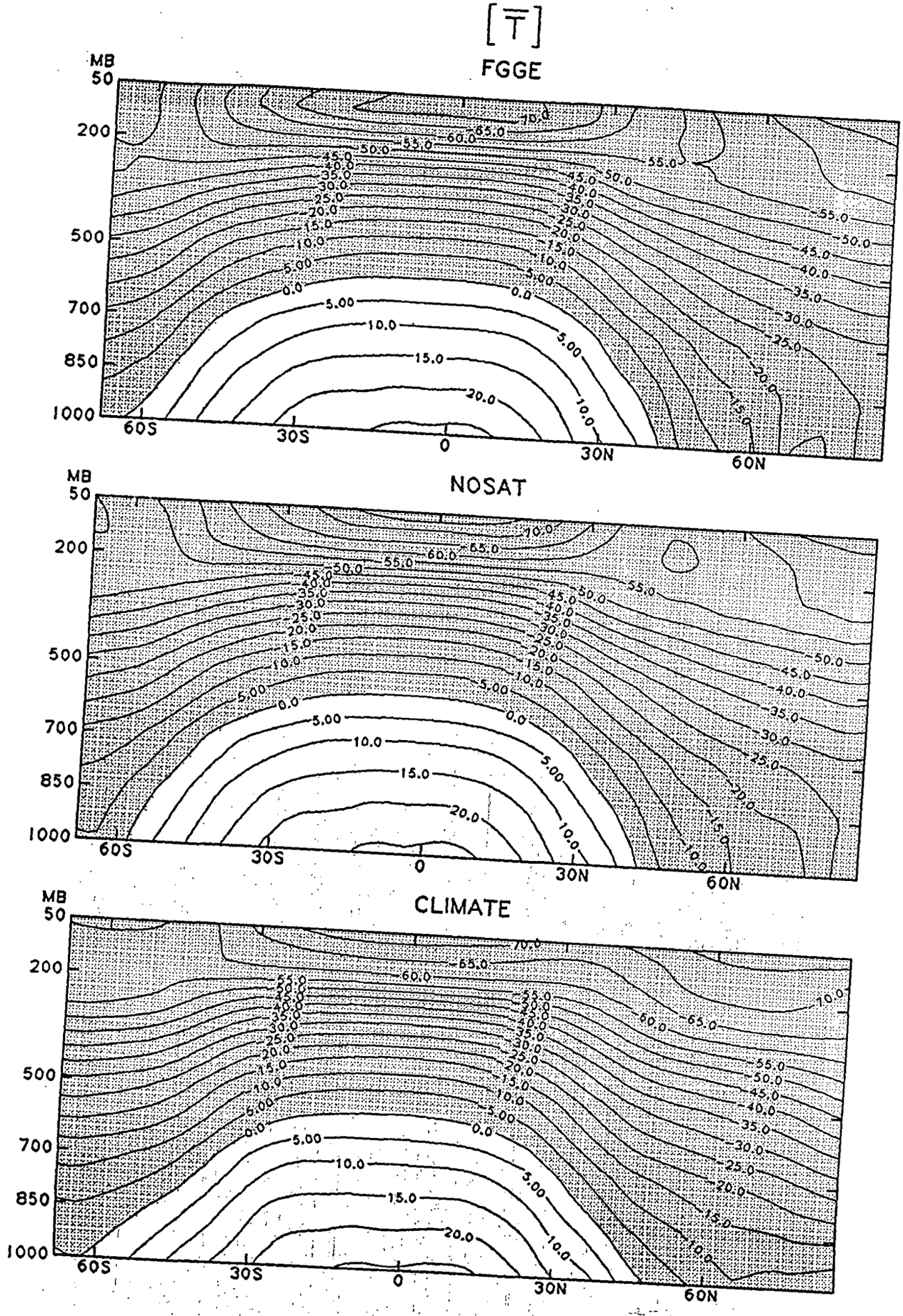

Figure 6. Zonally averaged temperature ($[\bar{T}]$) in °C for the FGGE, NOSAT, and CLIMATE analyses.

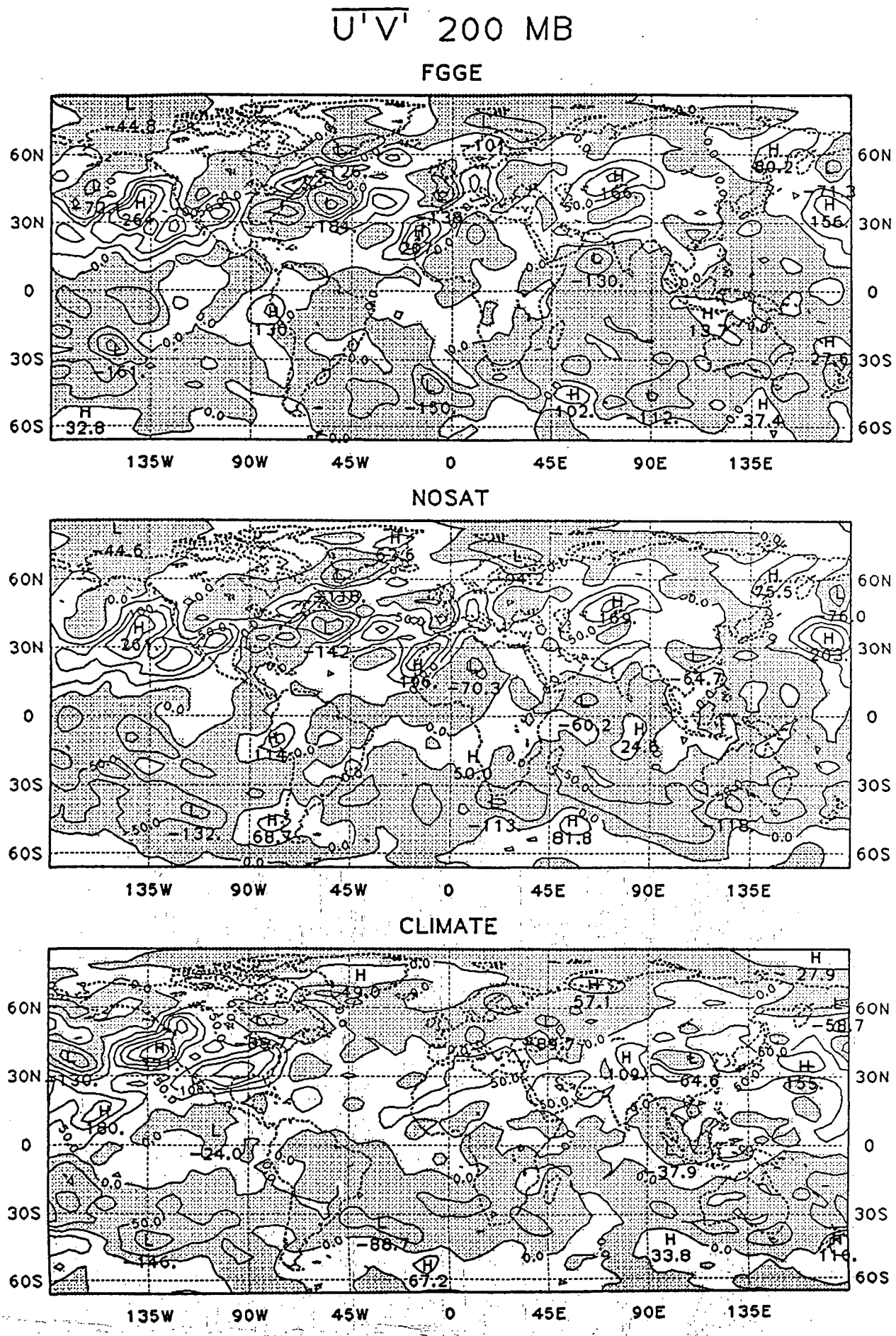

Figure 7. $\overline{u'v'}$ in m^2s^{-2} at 200 mb for the FGGE, NOSAT, and CLIMATE analyses.

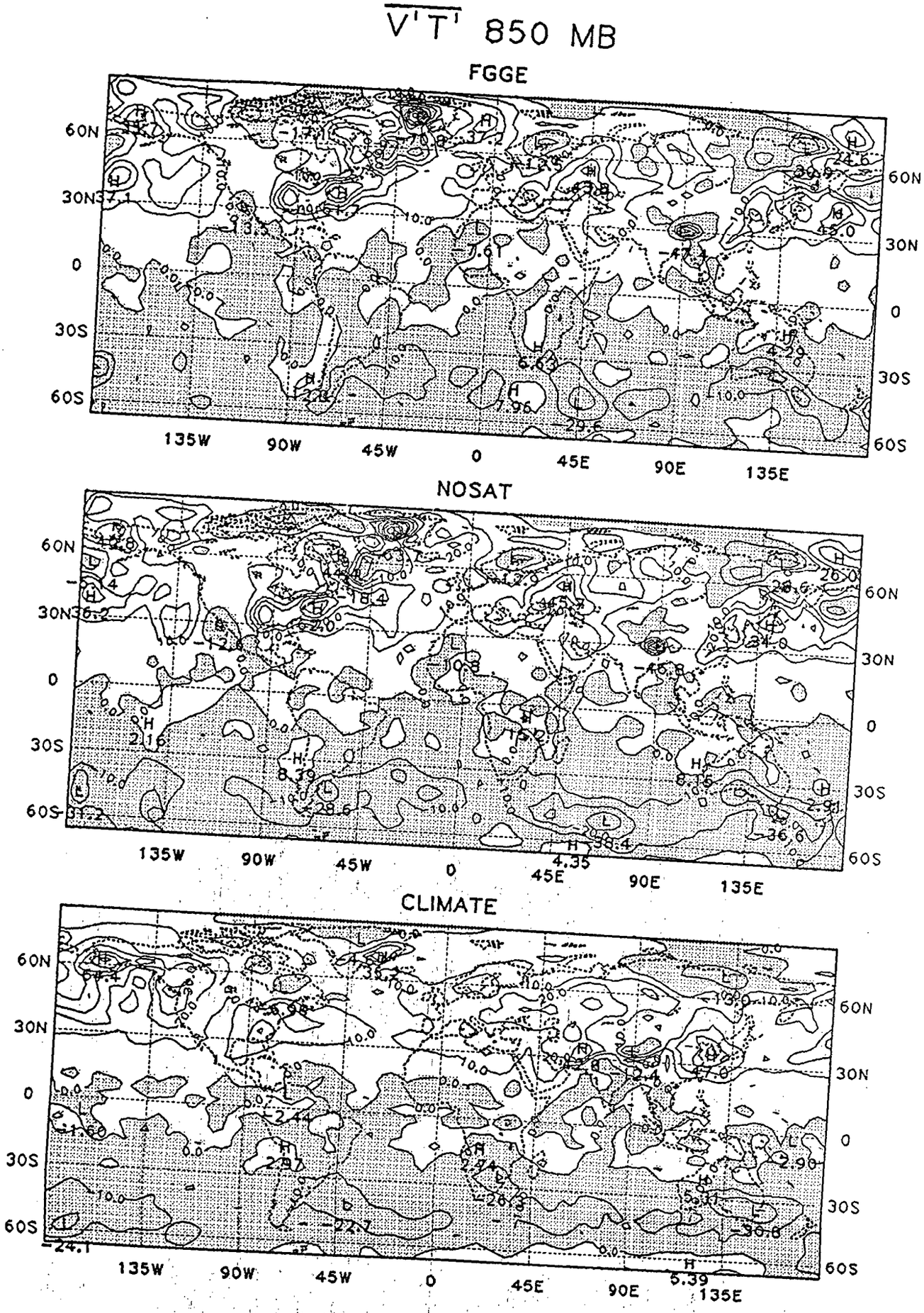

Figure 8. $\overline{v'T'}$ in m s^{-1} °C at 850 mb for the FGGE, NOSAT and CLIMATE analyses.

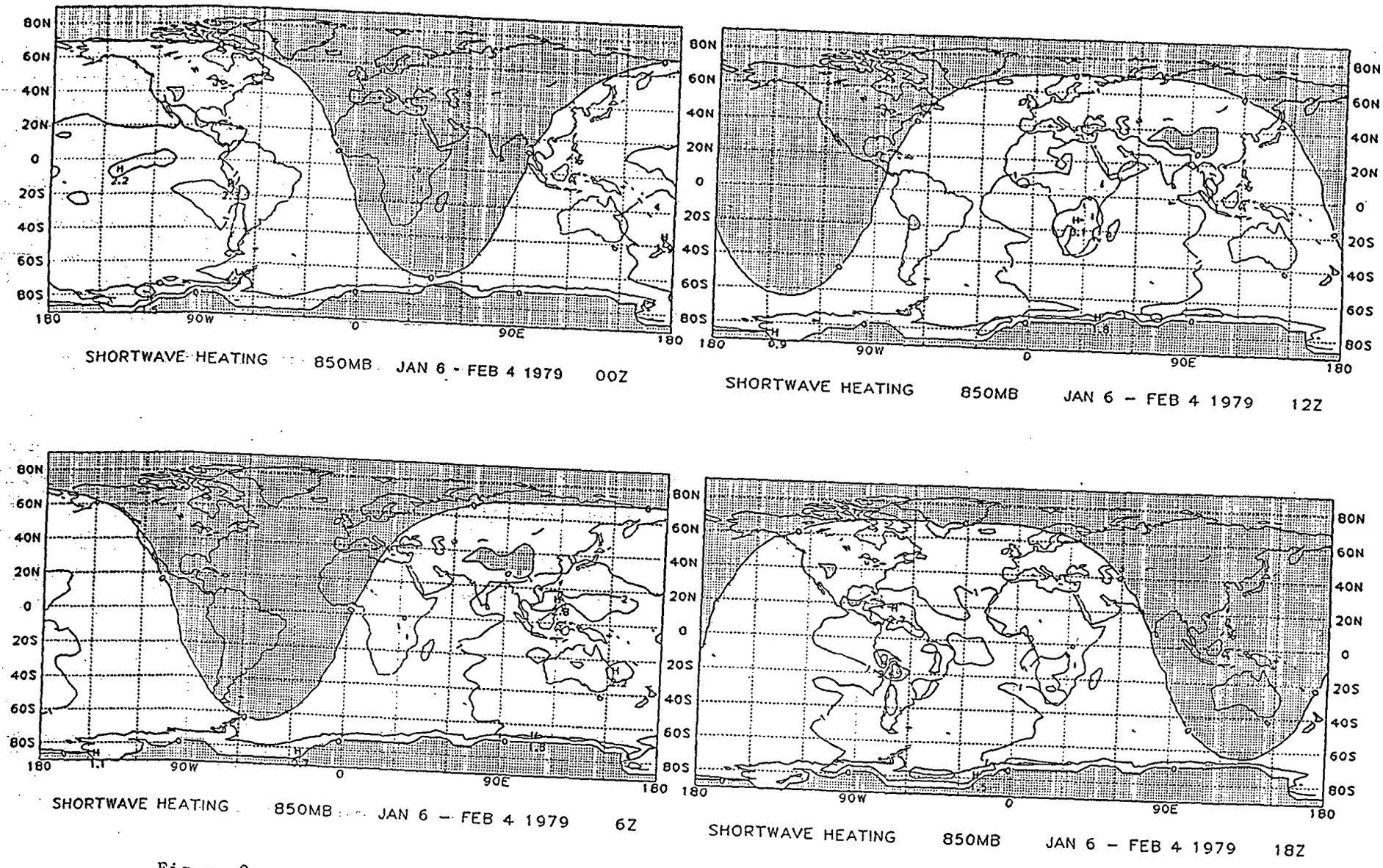

Figure 9. Heating due to shortwave radiation at 850 mb - 4 synoptic hours (°K day^{-1}).

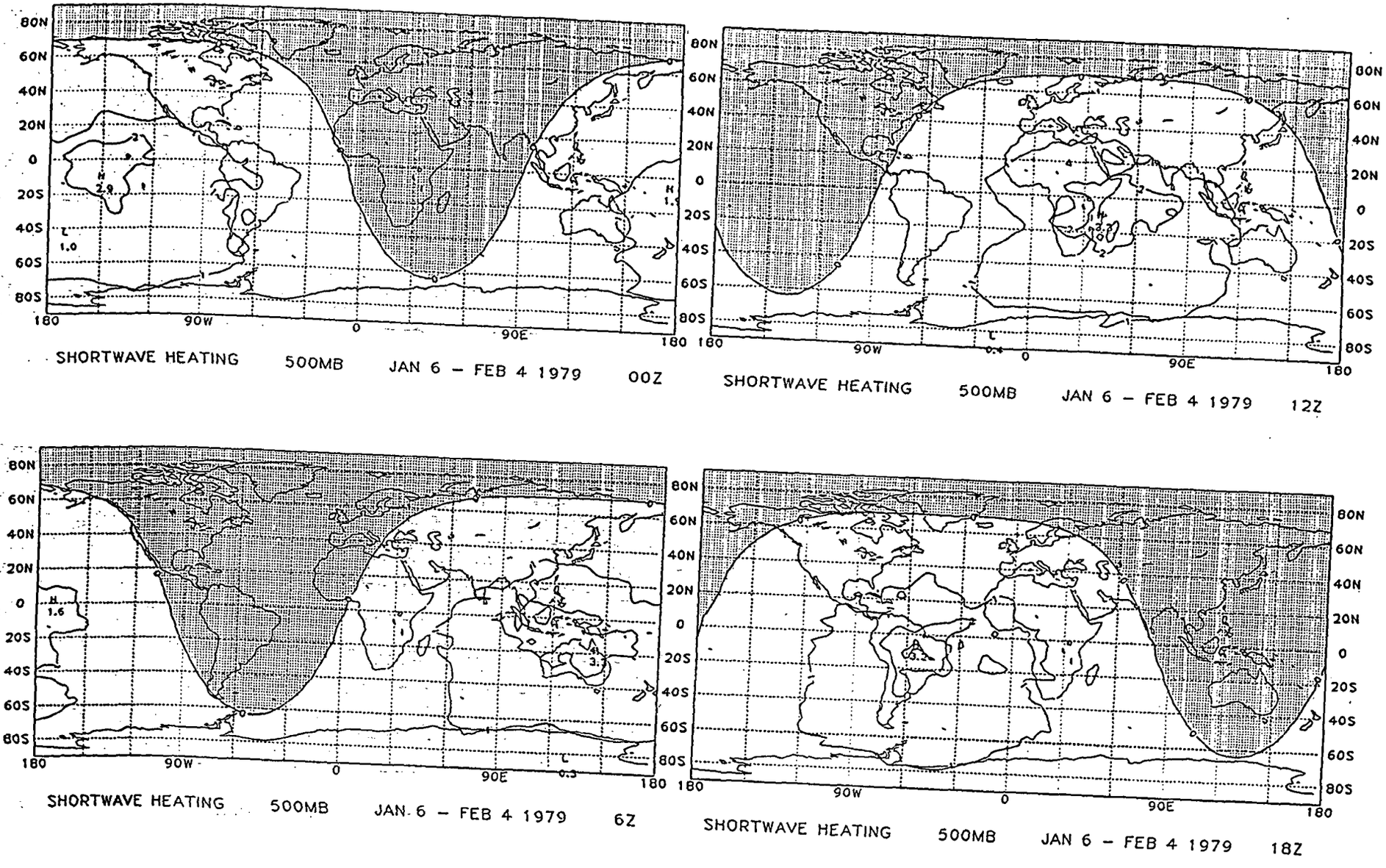

Figure 10. Heating due to shortwave radiation at 500 mb – 4 synoptic hours (°K day^{-1}).

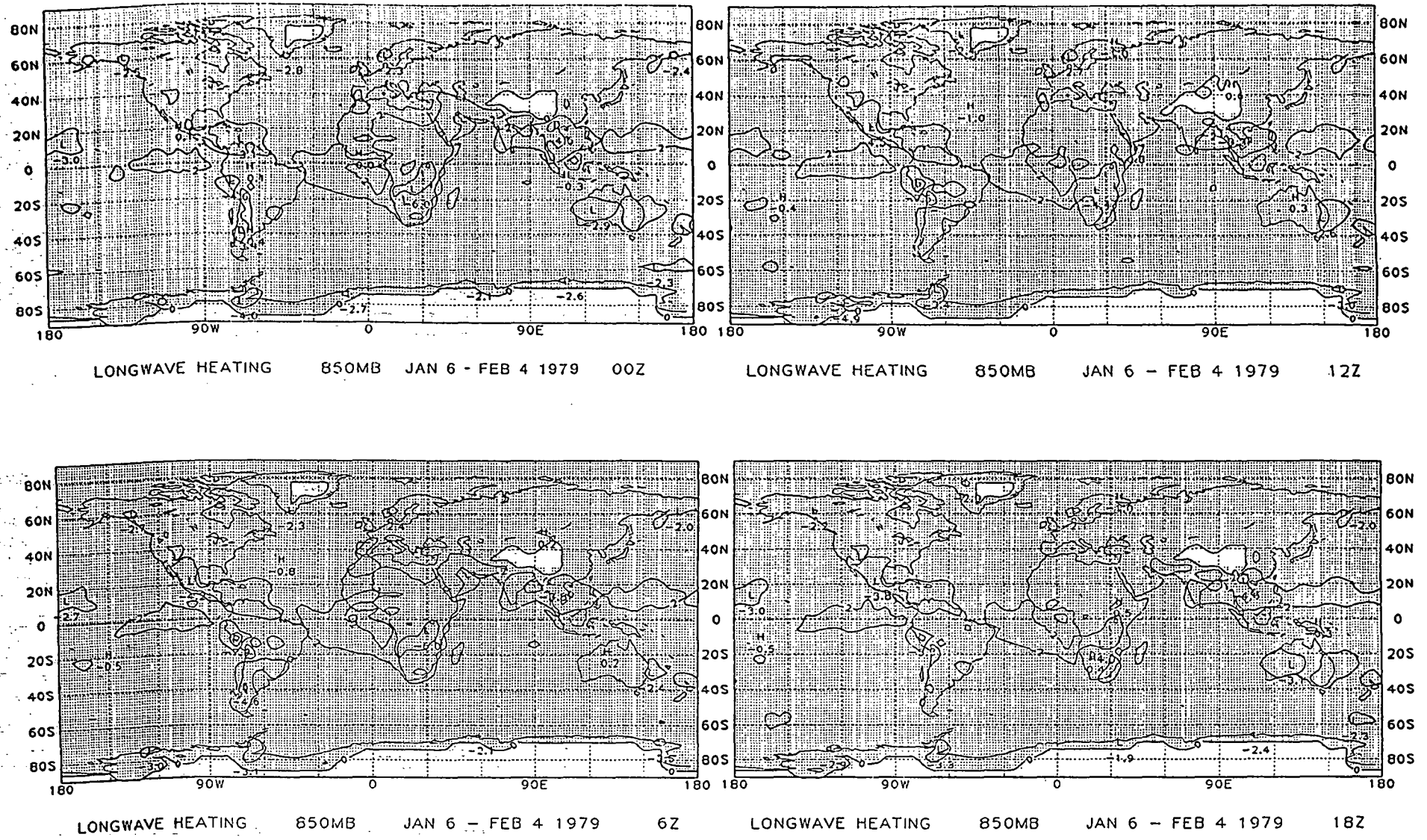

Figure 11. Heating due to longwave radiation at 850 mb - 4 synoptic hours (°K day^{-1}).

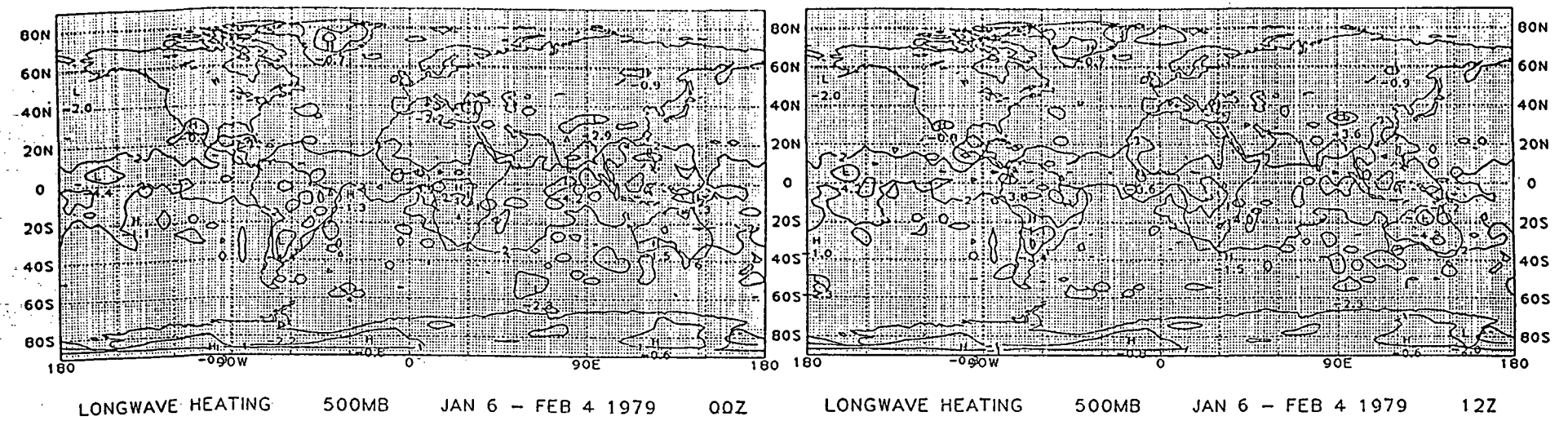

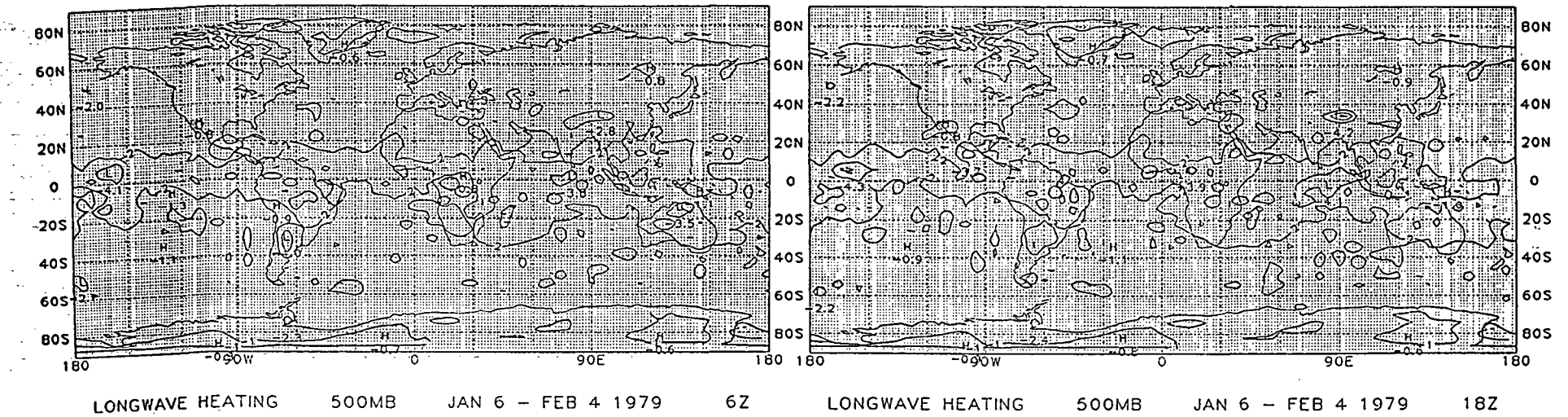

Figure 12. Heating due to longwave radiation at 500 mb – 4 synoptic hours (°K day^{-1}).

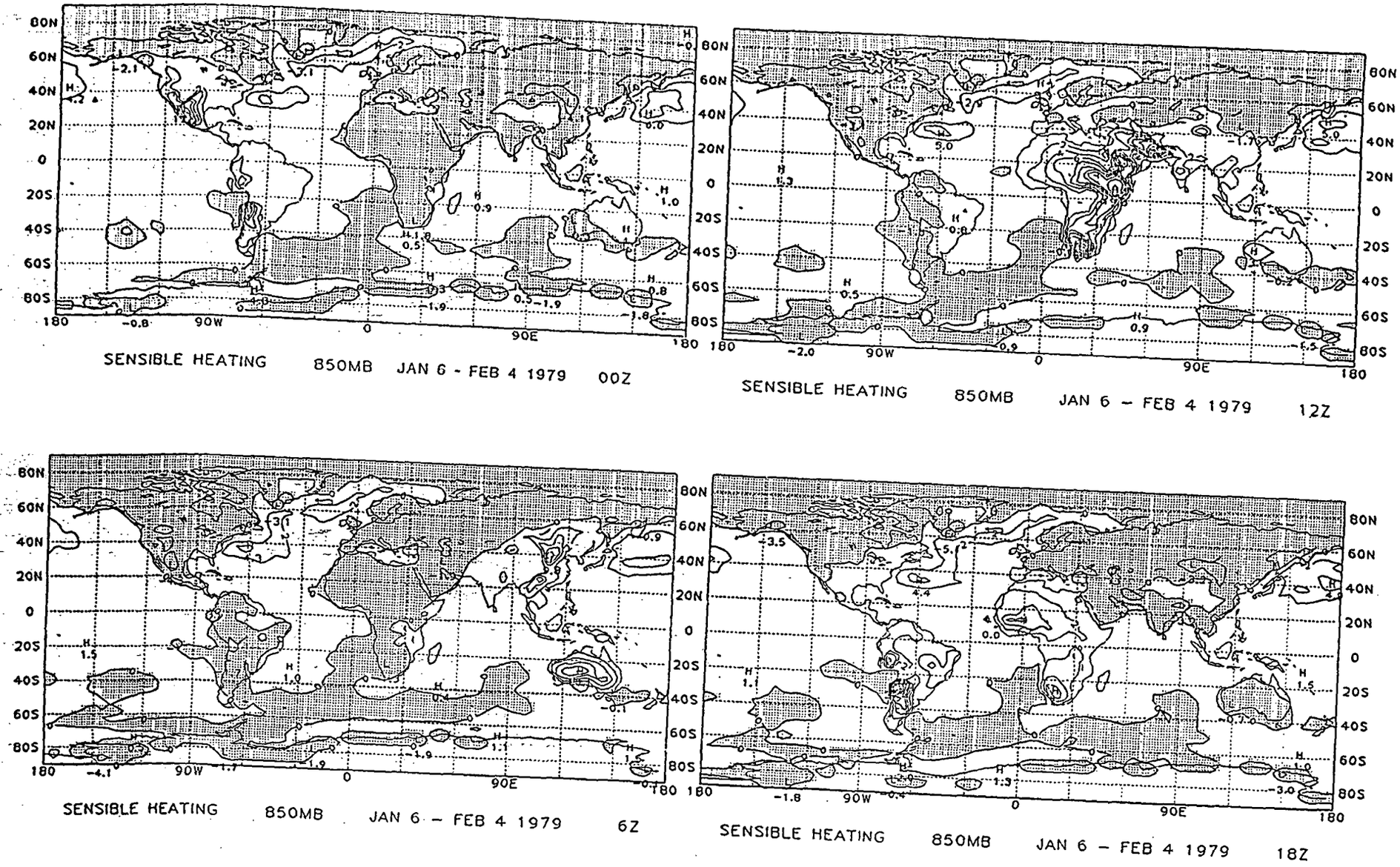

Figure 13. Sensible heating at 850 mb - 4 synoptic hours (°K day^{-1}).

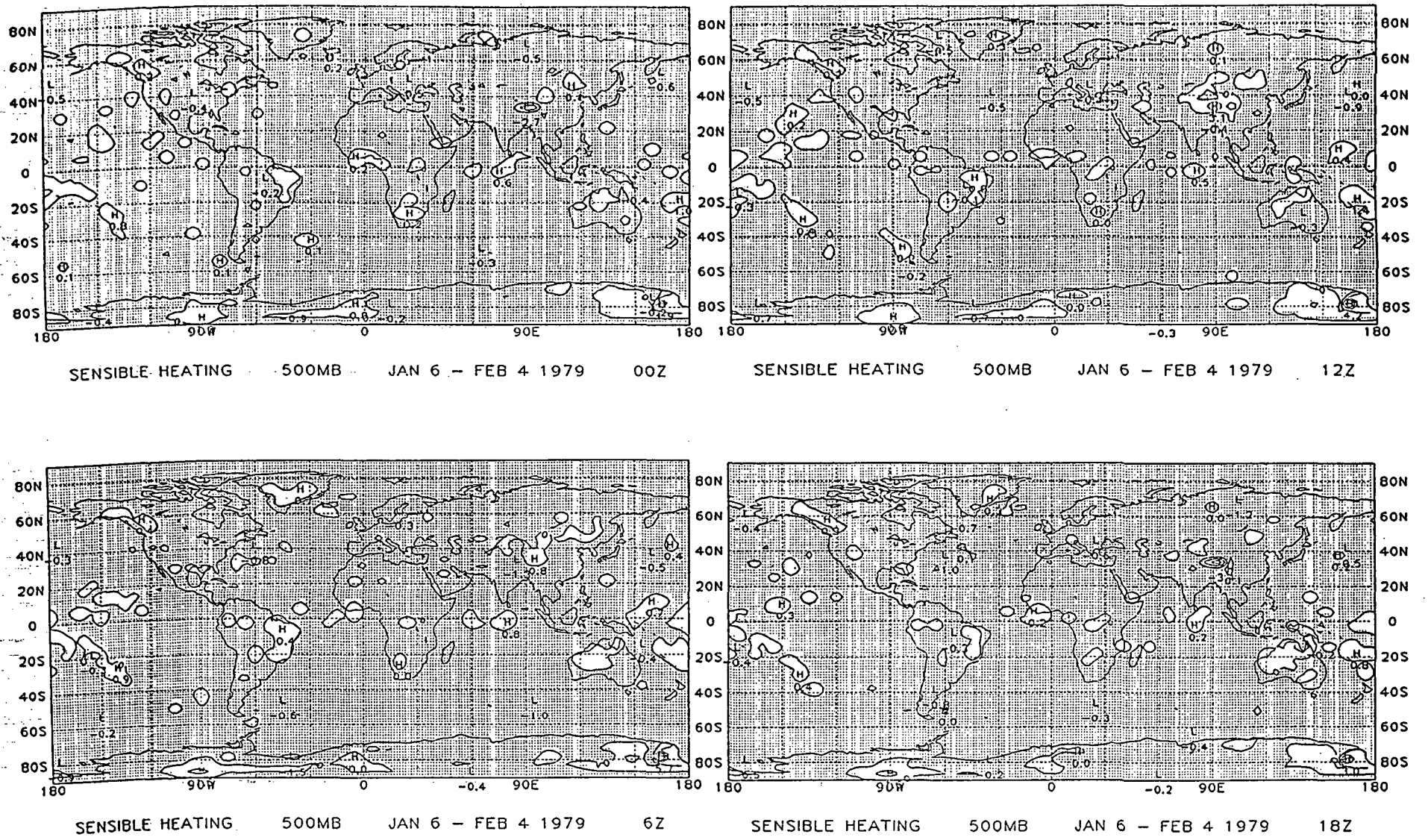

Figure 14. Sensible heating at 500 mb – 4 synoptic hours (°K day^{-1}).

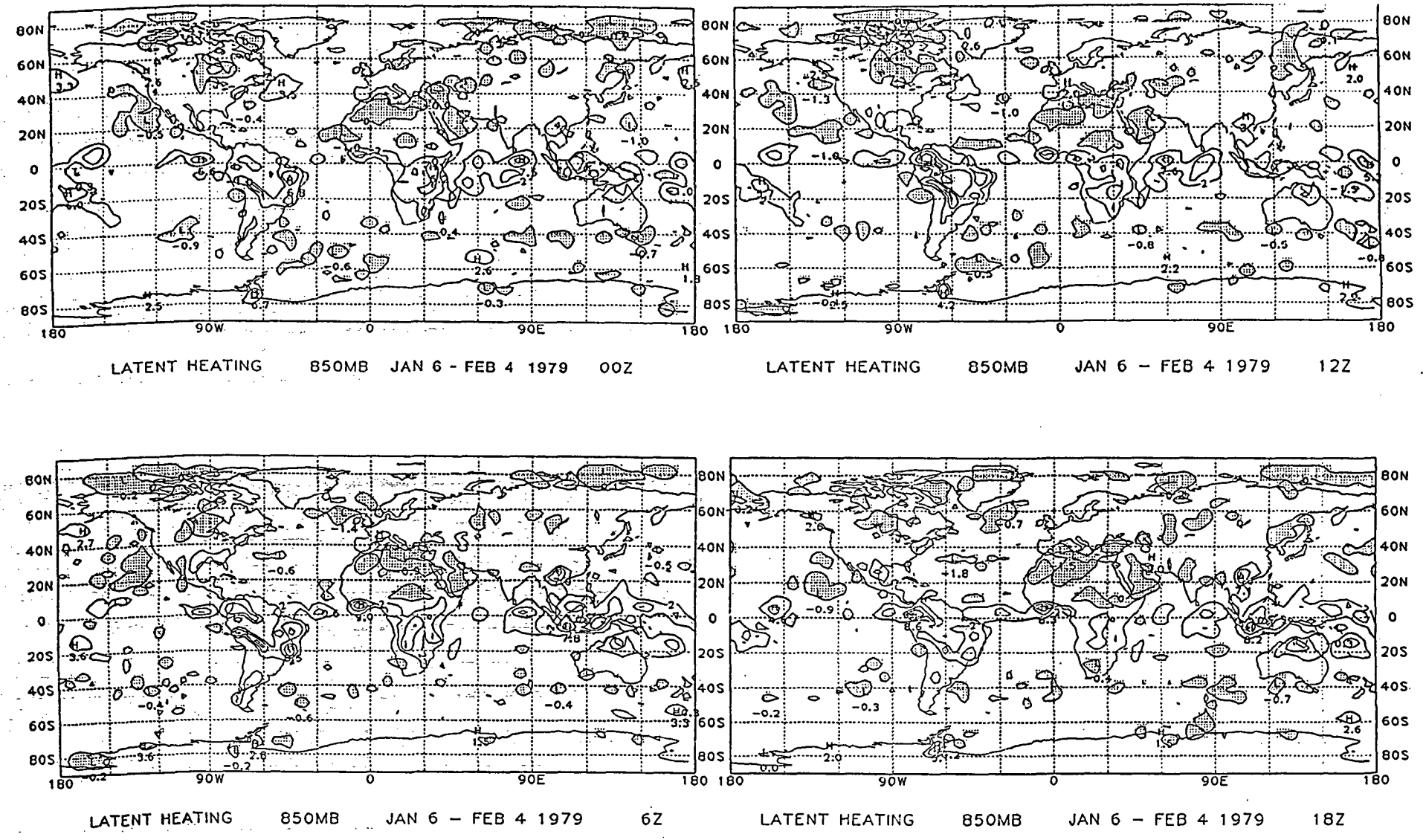

Figure 15. Latent heating at 850 mb - 4 synoptic hours (°K day^{-1}).

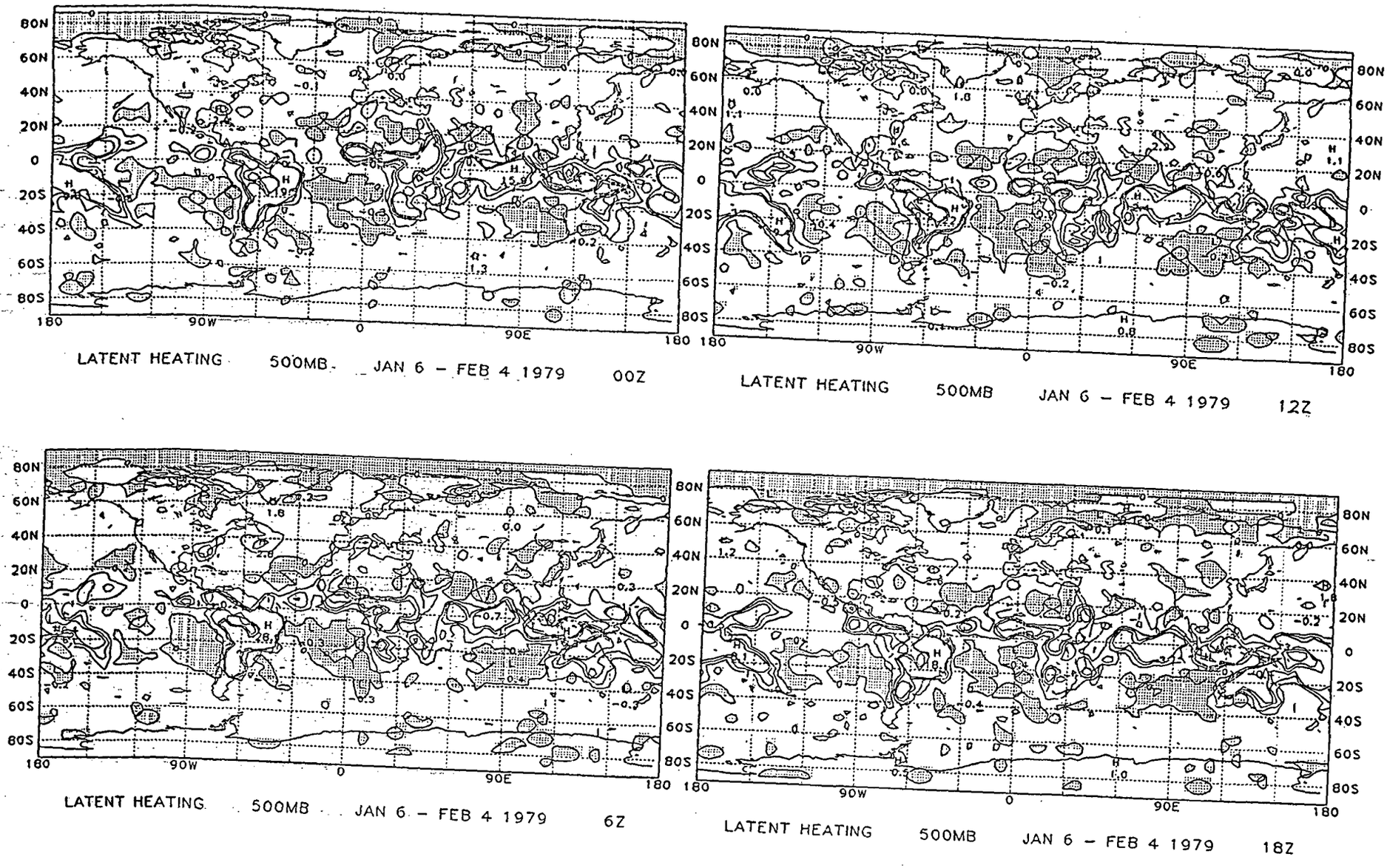

Figure 16. Latent heating at 500 mb – 4 synoptic hours (°K day^{-1}).

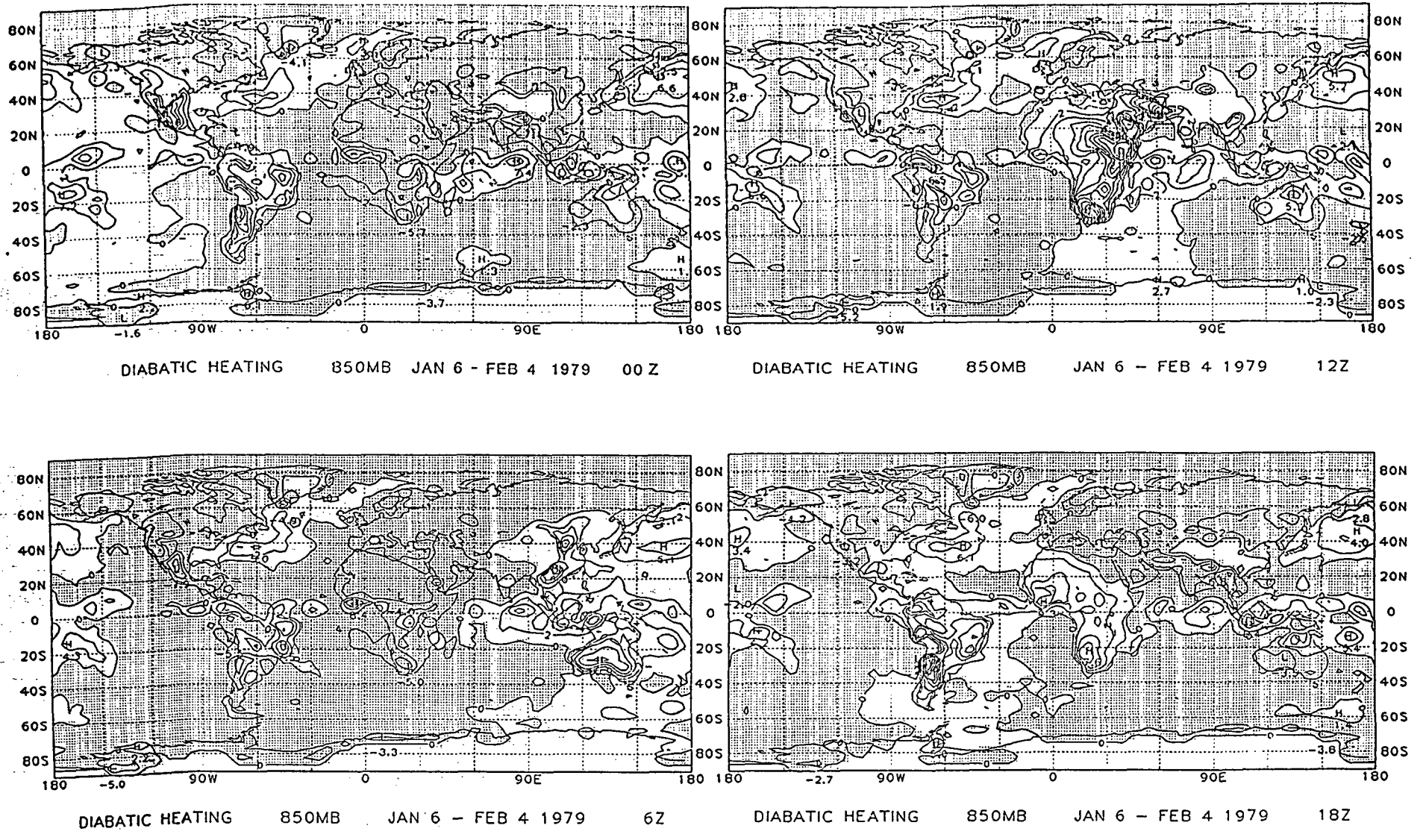

Figure 17. Total diabatic heating at 850 mb - 4 synoptic hours (°K day^{-1}).

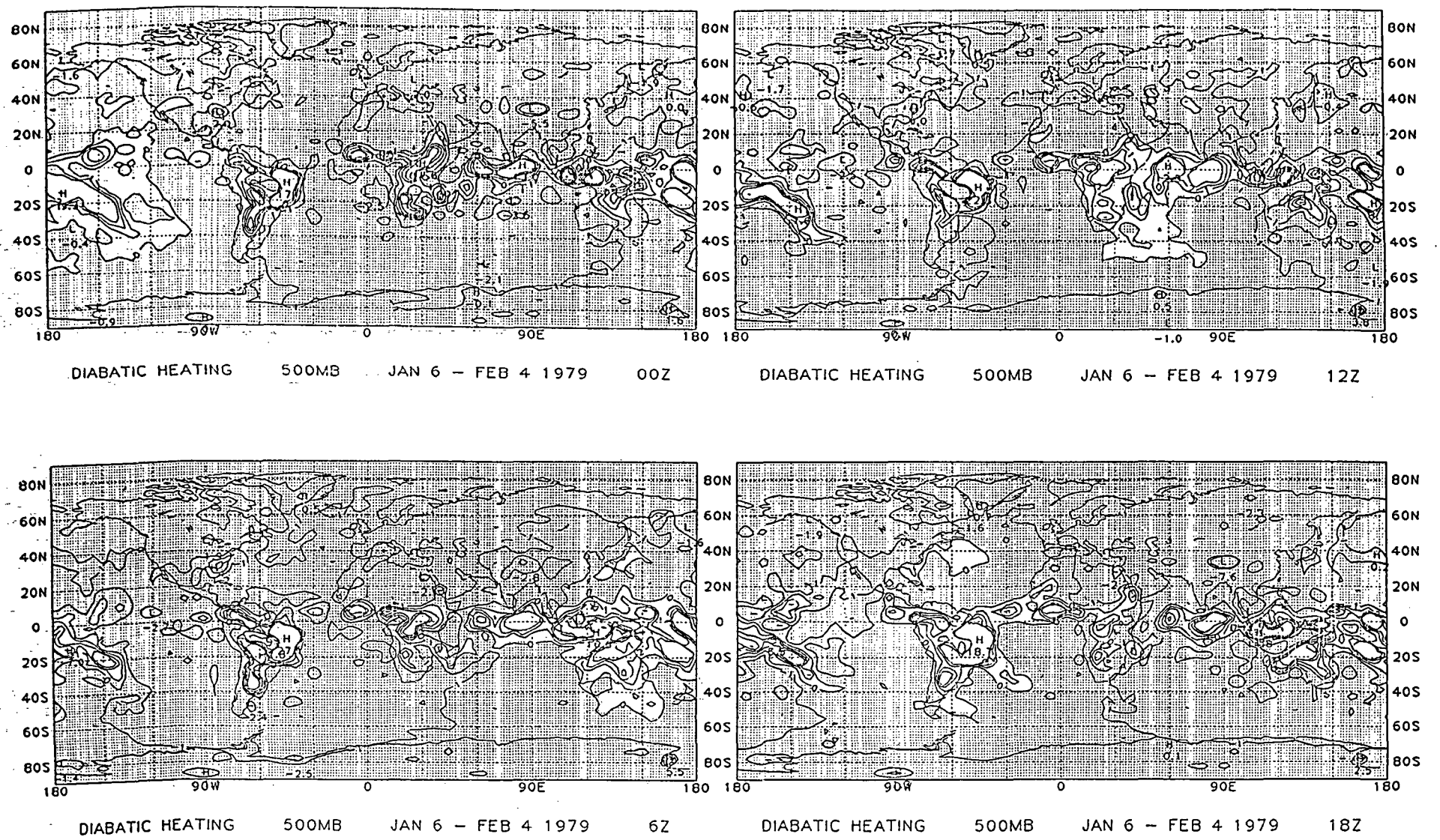

Figure 18. Total diabatic heating at 500 mb – 4 synoptic hours (°K day^{-1}).

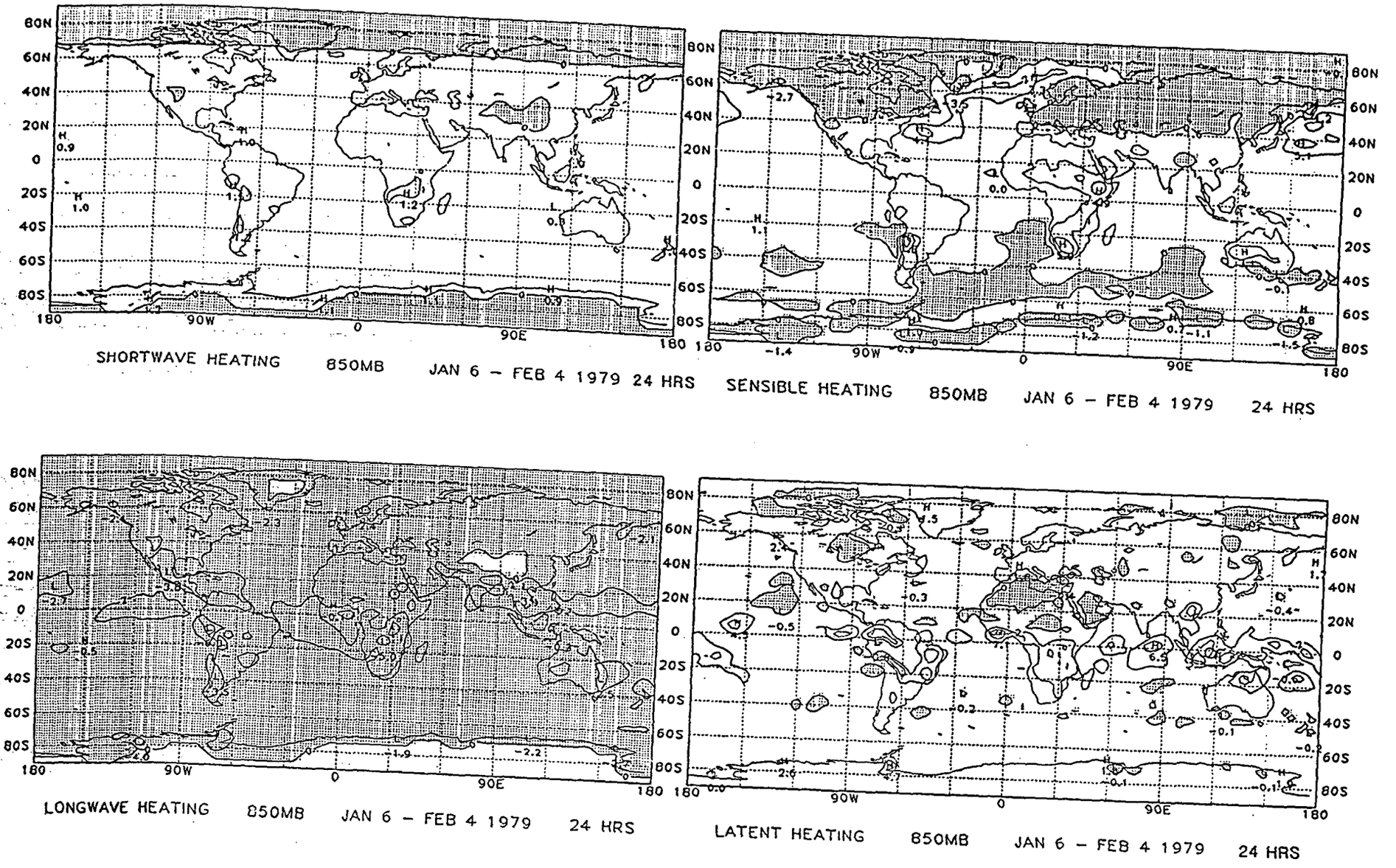

Figure 19. Four heating components at 850 mb combined for 24 hours (°K day^{-1}).

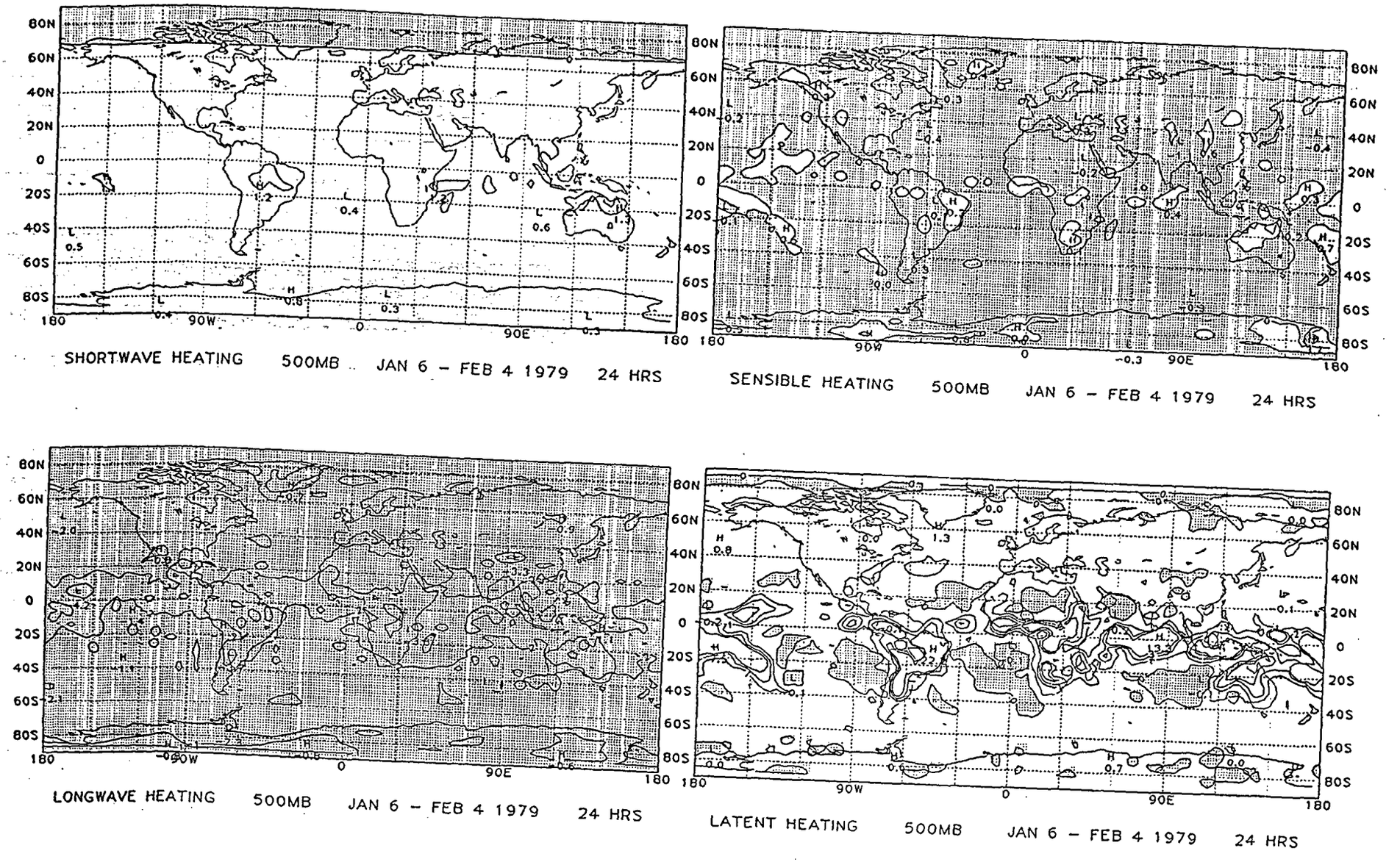

Figure 20. Four heating components at 500 mb combined for 24 hours (°K day^{-1}).

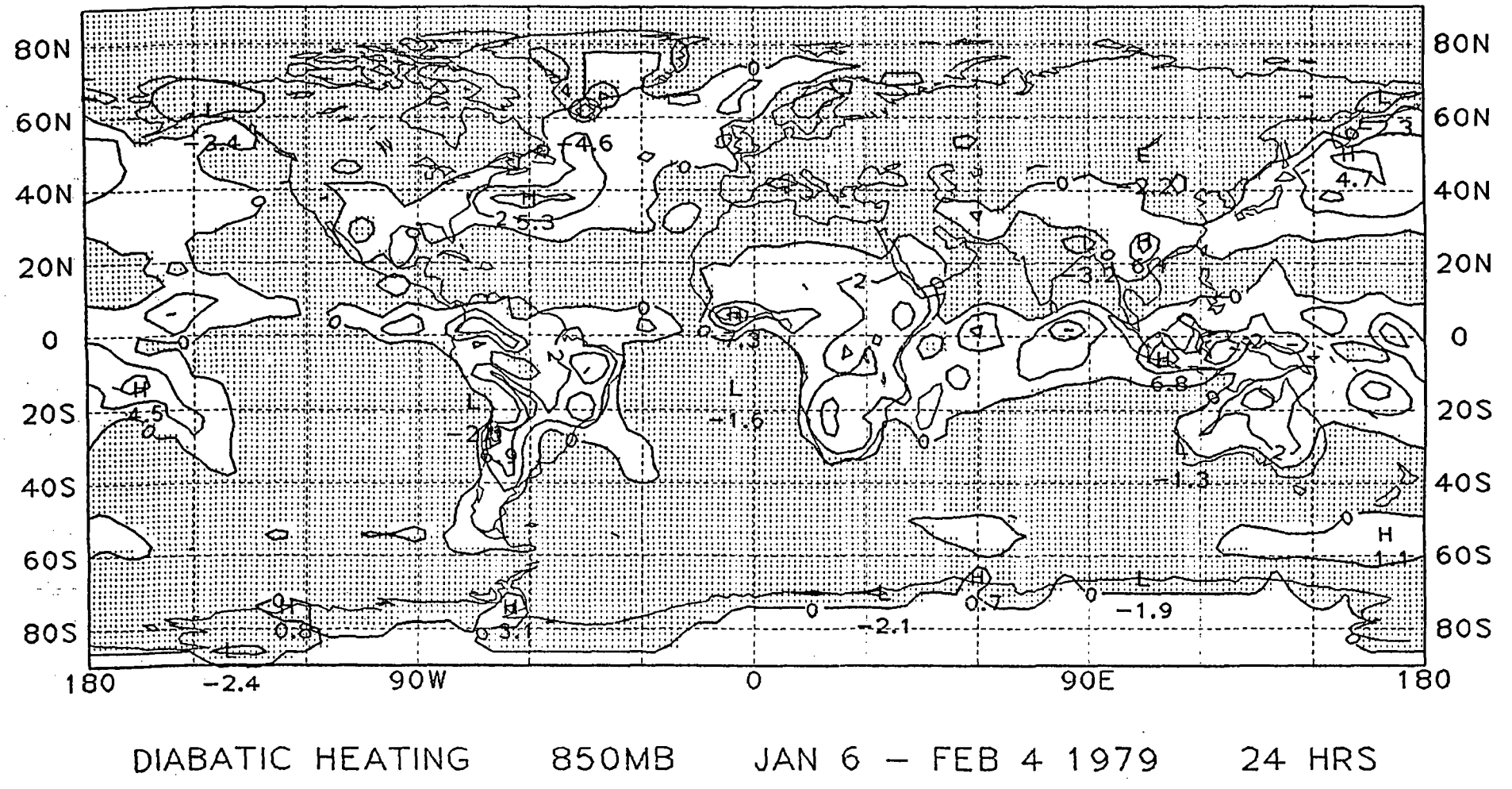

Figure 21. Total diabatic heating at 850 mb combined for 24 hours (°K day^{-1}).

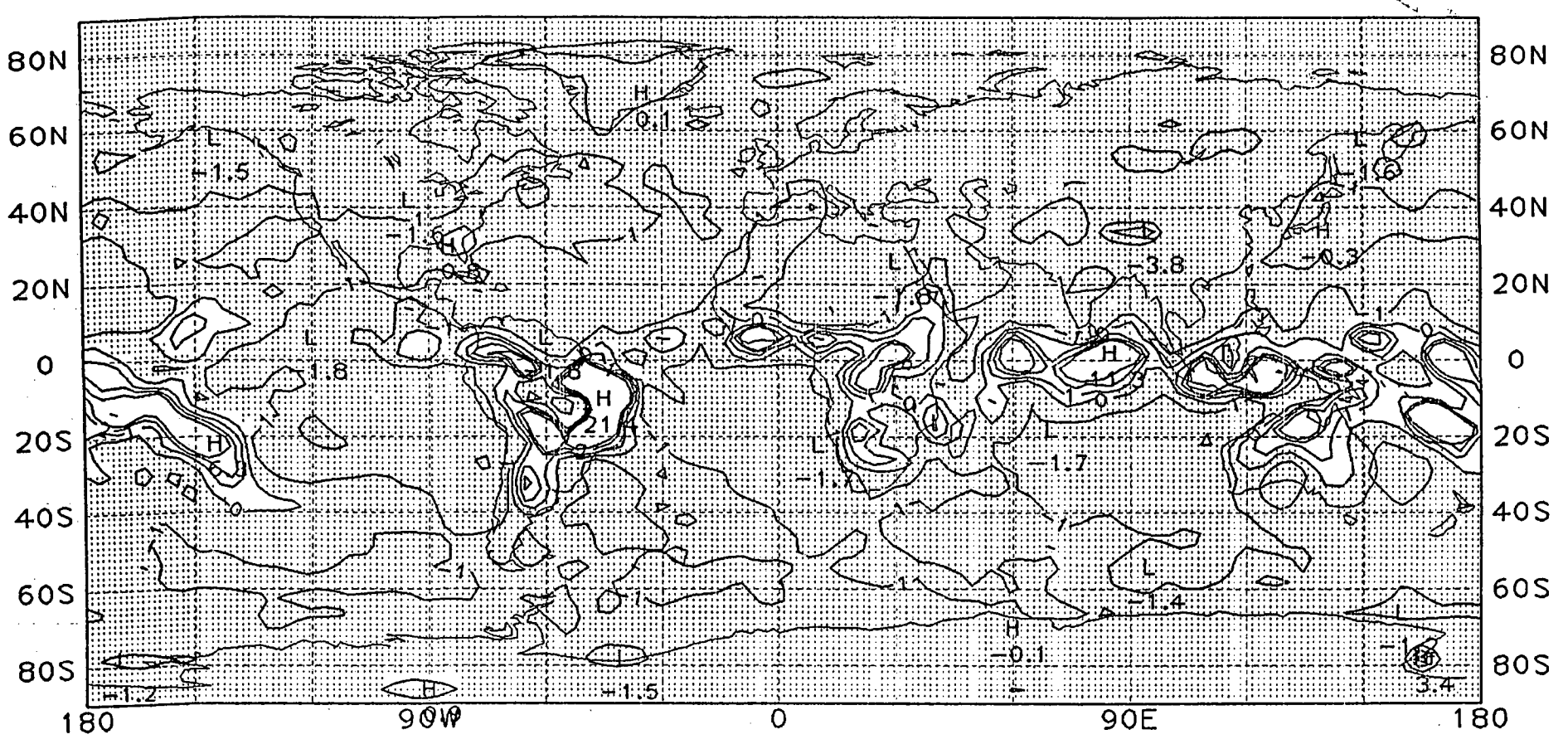

Figure 22. Total diabatic heating at 500 mb combined for 24 hours (°K day^{-1}).